

# Performance and Scaling of a Dense Plasma Focus Light Source for EUV Lithography.

Igor V. Fomenkov, Richard M. Ness, Ian R. Oliver, Stephan T. Melnychuk, Oleh V. Khodykin, Norbert R. Böwering, Curtis L. Rettig, Jerzy R. Hoffman  
(Cymer, Inc., 17075 Thornmint Court, San Diego, CA 92127).

Over the past several years, a continuous improvement of the performance parameters of discharge produced plasmas as potential sources of 13.5 nm radiation for commercial EUV lithography systems has been achieved. At Cymer we have continued developing the dense plasma focus (DPF) discharge as an EUV source. The majority of the data presented here is focused on DPF operation with xenon gas. We have recently started investigating the DPF operation with Sn, as well. A significant improvement in conversion efficiency (CE) was observed. We have investigated DPF configurations with different polarity of the drive voltage. Central to both configurations is the pulsed power system, which is being developed to operate in continuous mode at 5 kHz while delivering approximately 10 J to the load. Significant differences have been observed for the energy deposition profiles in the positive and negative polarity systems. Calorimetric data show that the fraction of energy deposited into each discharge electrode depends on the polarity. The thermal engineering of the central electrode remains a major challenge. With the present generation DPF we have demonstrated operation at 5 kHz in burst mode and at 2.3 kHz in continuous mode, with 76 W of in-band energy generated at the source. We observed that certain transient effects in the EUV output were correlated with the degree of energy coupling during the burst. However, we found that the pulsed power system is well matched to the load with >90% of the stored energy coupled to the discharge and electrodes. The conversion efficiency of the DPF operated with Xe is near 0.5% for both polarities, while measurements with Sn show a CE ~1.7%. Plasma modeling supported the optimization of the pinch dynamics and electrodes. Debris mitigation studies were also carried out and the carbon contamination was reduced.

**Keywords:** EUV Lithography, EUV light source, Dense Plasma Focus, Discharge Produced Plasma Light Source, Xenon Emission, Sn Emission, Negative Polarity Dense Plasma Focus.

## 1. INTRODUCTION

In order to meet the needs of future lithography systems in the extreme ultraviolet (EUV) a high-power light source is required for integration into a stepper tool based on reflective optics with multilayer (ML) coatings designed for highest throughput at a wavelength of 13.5 nm [1]. Over the past years Cymer has pursued the research and development of discharge produced plasmas (DPP) to meet the requirements of commercial high-volume manufacturing (HVM) tools. A dense plasma focus (DPF) configuration was chosen since it provides an open geometry with large possible collection angle and can be operated over a wide parameter range.

Progress on our source development has been reported annually in the past [2-5]. Here, we give an update and an overview on the present status of the EUV development at Cymer, discuss scalability issues and report on recent progress with our DPF source. Areas of investigation included pulsed-power development, thermal profiling, thermal management of electrodes, calorimetry, characterization of output power and source size, studies of burst mode operation at high repetition rates, plasma modeling and spectroscopy, analysis of debris and contamination issues and studies of Sn as an alternative source element. The DPF sources were operated with both positive and negative input voltage polarity in continuous and burst mode at high repetition rates.

Industry source requirements are in the range of 80 to 120 W EUV power (2 % bandwidth) at the exit focus of the source-collector module (the so-called intermediate focus). Other specifications agreed among

stepper manufacturers are repetition rates above 6 kHz, integrated energy stability ( $3\sigma$ , 50 pulses average) of  $\pm 0.3\%$  and a collector lifetime exceeding 10000 hours. Source etendue, maximum acceptance angle of the illuminator and spectral purity of the emitted radiation are not so precisely defined yet.

## 2. OVERVIEW OF SOURCE

The main features of our DPF machines have been described in detail in previous publications [2-5]. Using a reliable, all-solid state pulsed-power system that is scalable to high repetition rates (6-10 kHz) fast 4.2 kV pulses are delivered to the discharge with low inductance via a magnetic pulse compression scheme. The pinch event occurs in time near the current maximum (about 40 kA) at a location in front of the electrodes.

Although the majority of our development studies were carried out with xenon gas, we have also operated the apparatus with good success using metal fuels like tin and lithium. In order to address several areas of development in parallel in our investigations a number of DPF machines are in use focusing on different issues like plasma optimization, thermal engineering, power scaling, metrology and debris mitigation

Much of our past work has been carried out in a “conventional” DPF configuration with a positively biased central electrode (anode) and grounded outer electrode (cathode). In this configuration the discharge is preferentially initiated at the insulator located at the base of the electrode. We have found that in the positive DPF configuration at the conditions required for optimum EUV generation the gas does not break down when the anode voltage is applied. This necessitates the use of an independent pre-ionization plasma generator used for discharge initiation. Strong EUV generation with similar conversion efficiencies was also observed when a negative voltage was applied to the center electrode. The ions moving towards the inner electrode can be efficiently pinched and the energy dissipation at the inner electrode may be decreased since electron bombardment may be reduced. In contrast to operation with positive polarity the plasma initiation occurs in this case due to self-pre-ionization with the geometry similar to a hollow-cathode configuration. In agreement with other DPF discharges [6] the optimum pressure is found to be lower for the negative polarity DPF leading to a reduction of absorption by xenon gas.

One of the main tasks ahead is to identify paths to achieve higher EUV powers. The source output can be scaled by increasing repetition rate, conversion efficiency and collection efficiency. However, this requires improvements and optimization in different areas like pulsed-power system, thermal extraction, gas dynamics, electrode materials and geometry and pre-ionization system. Higher efficiencies may be attained by optimization of the plasma conditions and also by using better-matched source elements and collector designs with high acceptance angle and coatings for high reflectivity. As described below, significant improvements were obtained in most of these areas.

## 3. PULSED-POWER DEVELOPMENT

The power system development over this past year was focussed on system optimization and modifications necessary to support high rep-rate and high duty cycle operation. The schematic of the solid-state pulsed-power module is shown in Fig. 1. The module presently in use only has a single stage of pulse compression following the transformer. (See also Ref. [6]). By means of pulse-charging via a resonant charger from a set of parallel, 30 kW DC power supply modules, a nominal voltage of 1.3 kV is applied to the first energy storage capacitor  $C_0$ . Using parallel IGBT switches and the magnetic assist  $LS_1$  the charge is transferred to  $C_1$  and from there via a magnetic switch  $LS_2$  and a step-up transformer to the output capacitor bank  $C_2$ . After saturation of the magnetic output switch  $LS_3$  the stored energy is applied to the load in about 150 ns.

Experiments were conducted in an attempt to minimize the output circuit inductance and thereby maximize the peak output current and conversion efficiency. Two different hardware configurations were tested with one version resulting in an  $\sim 10\%$  decrease of the  $C_2$  capacitor bank inductance. In order to reduce the output inductance of the SSPPM further and to increase the peak current another magnetic pulse compression stage with ceramic capacitors is currently being designed.

Analysis of the power dissipation of the SSPPM indicates that operation at high repetition rates at high duty cycles necessitates air and water-cooling of the device components. Therefore, the thermal management of the power system modules was improved to support high-average power operation. Liquid-cooled cold plates have been designed to support operation of the DPF solid-state IGBT and diode devices. Liquid-cooled hardware is also being developed for the LS<sub>2</sub> and LS<sub>3</sub> magnetic switches and the transformer magnetic cores. Thermal Finite Element Analysis (FEA) models of the LS<sub>3</sub> core predict that the worst-case core temperature has been dramatically decreased through these design modifications and improvements. The maximum core temperature calculated previously was reduced by about 200 °C to a level of ~160 °C (based on nominal operation at 5 kHz, 100% duty cycle). This is compatible with long-lifetime operation of the magnetic cores.

#### 4. THERMAL PROFILING, THERMAL MANAGEMENT AND CALORIMETRY

As part of our development program we have constructed and calibrated a thermographic imaging system capable of providing time resolved electrode surface temperature measurements. Electrode temperatures were measured for similarly configured DPF systems operated with un-cooled electrodes in positive and negative polarity mode. The DPF systems were operated in a burst mode at 800 Hz with several hundred pulses per burst and inter-burst times of several seconds. Several bursts were required to heat the electrodes to the point of visible emission where the thermography system was designed to operate. The typical operating range of the thermographic system was 650 °C to 2000 °C. The data were collected a few microseconds after the plasma was extinguished.

Surface temperature distributions for the different polarity cases were measured using identical electrodes. Operating conditions were optimized to produce the highest in-band EUV for each configuration. In both cases, significant heating occurs on the inside, near the top of the inner electrode, however in the positive DPF case, the exit aperture of the gas orifice is also significantly heated. The inner electrode of the positive DPF also receives a larger fraction of the total energy than does the negative DPF. The maximum temperature measured on the positive-polarity DPF after the 3 kJ burst was ~1250 °C, while for the negative DPF the highest temperature was ~900 °C.

Several factors contribute to the heating of the source during operation: Energy is transferred from the plasma by radiation to the electrodes, the chamber and the debris shield/collector assembly. Heating by conduction from the plasma and Ohmic heating of the electrodes also leads to sizable energy transfer.

Thermal engineering of the discharge region of our DPF light source has progressed significantly over the last year. Higher steady state repetition rates, up to 2,300 Hz, have been demonstrated with a total energy of > 28 kW removed from the electrodes and the vessel including coolant pumping power. New designs for inner and outer electrodes and several insulator configurations have been developed.

Three cooling designs have been successfully fabricated and tested for the inner electrode. These are open annular channels, porous-metal and micro channels. Externally these electrodes are similar in appearance and are fully interchangeable, however internally the heat exchangers are distinctly different. Lifetimes up to 35 million pulses have been demonstrated with the end-of-life characterized by non-catastrophic coolant leakage. The ultimate performance is still unknown, as failure due to excessively high thermal loads has not occurred. Computer simulations have been updated using empirical data to more accurately model the detailed thermal loading on the electrode. The resulting temperature distribution calculated for the electrode shows good correlation between areas of high temperatures in the model and those of highest erosion observed in experiments.

The open annular-channel cooled electrode has removed >11 kW of heat, this includes the hydraulic coolant pumping power in addition to thermal loads associated with DPF operation. Coolant has been pumped through this device at up to 38 l/min with entry pressures approaching 6,200 kPa. The porous metal design uses less coolant and has a higher pressure drop through the device while the micro-channel

design has an operating point somewhere between the two. All three designs were tested to at least 2,000 Hz and the open-channel device has been run at a steady-state repetition rate of 2,300 Hz.

A new design of outer electrode has been developed. Among other features salient to the gas delivery and plasma initiation it has simplified the coolant plumbing and improved the assembly and the serviceability. Furthermore it incorporates cooling for pulsed-power output components. Testing has confirmed improved water flow characteristics through the device and better vacuum performance.

Discharge insulator development has progressed and UHV elastomer-free designs have been fabricated with satisfactory vacuum, high-voltage and thermal performance. Lifetimes of the insulators currently exceed those of the inner electrodes. Erosion of the tungsten inner electrode limits life between rebuilds of the system.

Thermal modeling predicts manageable inner electrode temperatures for up to 3 kHz operation with our first-generation cooling design using a flow partition inside of the electrode. As shown in Fig. 2, with the demonstrated water flow rate of 38 liters/min a thermal load of 12 kW can be supported at 3 kHz repetition rate. The next figure displays a comparison of the modeling results for uniform distribution with the case when the actually measured electrode temperature distributions are used as input to derive the heat flux. This leads to a doubling of the calculated wall temperatures. However, the maximum temperature on the electrode surface of these profiles coincides with the region where maximum electrode erosion was observed.

Thermal measurements were carried out for operation at high continuous repetition rates with both positive and negative applied voltage. As a function of repetition rate Fig. 4 shows calorimetric data of the total extracted power for thermocouple sensors at different positions at the inner and outer electrode and the chamber as well as a comparison of the removed power for both polarities. The distribution of heat removal indicates more favorable results at negative polarity of the inner electrode, since it takes a smaller relative share of the total heat in this case.

## 5. METROLOGY

Spectrally resolved measurements and characterization of the angular stability of the DPF operated with He-Xe mixtures were described in detail previously [5,8]. Further improvements have now been obtained for true in-band diagnostics. Considerable effort has been devoted to the development of absolute energy and imaging measurements for only the in-band radiation. We have found that pinhole source imaging systems utilizing on axis detection schemes were prone to underestimating the source size due to the presence of high energy photons that were not attenuated by the filter foils. For on-chip image integration in burst mode we found the appearance of local “hot spots” in the pinch. These high-energy emission regions preferentially weighted the calculated source size toward smaller sizes. Correlation measurements between the energy measured with an in-band energy monitor and integrated CCD signals showed significant disagreement. We believe this was due to the different spectral content of the signals on the two detectors.

Therefore, we have modified our source imaging diagnostic to include a ML mirror with an incidence angle of 45° after the pinhole and filter foils. This arrangement is shown in Figure 5. A comparison of in-band energy measurements using the absolute energy arrangement with the photodiode and the integrated CCD signal is shown in Figure 6 on a pulse-to-pulse basis. We observe almost perfect correlation of these two signals. This gives us confidence that the source images and corresponding emission volumes inferred from these images are more accurate than those obtained from the direct imaging configuration.

## 6. OPERATION AT HIGH REPETITION RATES

In a configuration with un-cooled electrodes, we have demonstrated DPF operation (at positive input polarity) of 5 kHz. Fig. 7 shows a burst of pulses for a particular gas mix. The shape of the characteristic

transient occurring at the beginning of each burst is highly dependent on operating conditions like electrode geometry, gas recipe and pre-ionization system.

We have observed a strong correlation between the EUV output energy and the degree of coupling of the stored energy to the discharge pulse. Fig. 8 shows the actual capacitor discharge waveforms, and photodiode waveforms during a 4 kHz, 300 pulse burst in a positive polarity DPF. We can clearly see that the degree of energy recovery during the burst can vary significantly. Fig. 9 gives an illustration of the correlation between the EUV output and the recovered energy. For the pulse-to-pulse development during a burst we find significant changes in the energy coupling. For many of the gas recipes used to produce high EUV output the coupled energy is in excess of 90% during the burst. The observed effects may be due to electrode heating during the burst that results in a change of the local gas density near the inner electrode. These effects are most pronounced for the non-cooled electrodes used in studies of the electrode geometry; however, they may also be expected to occur for the water-cooled electrodes during start-up transients.

These data show that the EUV in-band energy stability is strongly affected by the details of the discharge formation process and energy coupling mechanisms. These effects are still not fully understood and point to the need to develop a better fundamental understanding of the physical process in the discharge.

We have measured the EUV in-band energy output and source size in operation at a steady repetition rate of 2 kHz and for negative polarity. The EUV detectors and the data recording instrumentation have been described previously [4]. Using an EUV output monitor with debris suppression tube, in-band output energies of 38 mJ/pulse (into  $2\pi$ , 2% band width) were observed, corresponding to 76 Watts continuous average output power. In-band source size measurements were carried out using the imaging set up shown in Fig. 5. The results show that the average source size at the highest output power was 3.0 mm x 0.4 mm (FWHM). For xenon injection into a low-pressure buffer gas, a more spherical source volume can be produced.

## 7. CONVERSION EFFICIENCY AND ALTERNATIVE TARGET ELEMENTS

Our efforts in DPF source development for the past few years have been primarily directed at optimization of the positive polarity DPF (PDPF) with Xe gas. Significant improvements in output energy have been realized by refining electrode geometries, gas recipes, and plasma initiation schemes. The trend in output energy and conversion efficiency (CE) was already summarized previously for various changes to the PDPF system [5].

Over the past 18 months significant progress has been made in optimization of the negative polarity DPF (NDPF) configuration. As mentioned previously the NDPF has a substantially different energy deposition profile compared to the positive machine. This makes the configuration easier to cool and leads to reduced electrode erosion rates. The possibility of operating the NDPF in a self pre-ionizing mode also allows for simplification of the power system. A potential drawback of the self-pre-ionized NDPF configuration is an increased amount of jitter between the application of the electrode voltage pulse, and the onset of the discharge. These effects can be mitigated by use of a simplified pre-ionization scheme compared with the PDPF.

A comparison between the EUV in-band energy of the positive and negative polarity systems, and the CE for operation with Xe is shown in Figs. 10 and 11. The slopes of the EUV energy versus dissipated energy curves for the best PDPF and NDPF curves are approximately equal, however, higher pulse energies were achieved on the NDPF system due to a higher available input energy. The leveling-off for the curve of NDPF efficiency versus energy is not as distinct for high input energies as in the case of the PDPF system.

Even with the improved performance obtained with the NDPF configuration it is clear that no significant improvement in efficiency was achieved so far. In order to reach the required EUV power levels of ~ 120 W at the intermediate focus point of the EUV source collector optic a substantial improvement in CE is still required. This has prompted us to investigate alternative elements as potential EUV sources. We had previously demonstrated that the DPF source could be operated with a variety of gaseous as well as solid

element sources such as Li. Recent experiments have concentrated on developing a delivery system for investigating the behavior of Sn in the discharge. We have successfully delivered Sn to the NDPF and measured the EUV in-band energy, CE, and the emission spectrum. Figure 12 shows a comparison of spectra obtained with the transmission grating spectrometer described previously [5,8] for operation with Ar only as well as for a mixture of Sn and Ar. The spectrum clearly shows the appearance of an emission line at 13.5 nm when Sn is added to the DPF. The CE for these data was approximately 1.7 %. Work in this area is being continued in order to obtain further CE improvements. Figure 13 shows a comparison between the typical EUV source size obtained with Xe and that obtained with Sn and Ar mixtures. The source emission spot with Sn is seen to be more spherical than that obtained with Xe gas.

## 8. PLASMA MODELING

The MHRDR magneto-hydrodynamic solver code has been adapted to the pinch geometry to provide a more solid understanding of the effects of geometry and drive circuit [9]. A time-dependent circuit model of the driver is used interacting self-consistently with the plasma load, calculated from a fluid description of the plasma. The description includes thermal conduction, radiation, ionization, and material properties in an equation of state formulation. Figures 14 and 15 show the calculated radial kinetic energy and discharge current as a function of time during the discharge. The various curves in the figure show the dependence of these quantities on the central electrode length. The radial kinetic energy peaks at the instant of the plasma pinch, and its magnitude is a measure of the coupling efficiency into directed kinetic energy. Thus, the existence of a length for which the kinetic energy is maximized represents the best transfer of energy from the magnetic field behind the pinch to the plasma internal energy. At this length, the timing between the pinch is optimized to that of the discharge circuit, whose time constant is fixed by external reactances. Thus the circuit and gross electrode geometry can be optimized for best plasma performance.

## 9. DEBRIS MITIGATION AND CONTAMINATION STUDIES

The lifetime of the first collection mirror is of major concern for all EUV light sources. In principle, discharge-produced plasmas can generate the following types of debris: Fast ions and neutrals from the source fuel, fast ions and neutrals from the electrode material as well as slower particles from source fuel, electrode and insulator material. Mono-atomic species and also larger particle assemblies (clusters) can occur. Even if the debris is effectively shielded the optics lifetime of the collector can still be limited by degradation due to contamination. Oxidation due to residual water vapor content can occur as well as carbon growth on the mirror surface induced by cracking of hydrocarbons under intense DUV and EUV irradiation.

A significant portion of our EUV development program is related to addressing the debris mitigation and environmental control issues related to maintaining a clean collector optic. We have been working on continuous upgrades to the DPF source to eliminate all elastomer seals in the vacuum system, and to eliminate all potential sources of hydrocarbon out-gassing. Previously, we reported results obtained with a multi-channel array simulating a debris shield [5]. This showed that the rate of EUV-catalyzed carbon deposition significantly exceeded the rate of all other sources of debris generation. These results were obtained with a DPF system having several elastomer seals, as well as containing some organic insulators. At that time residual-gas analyzer (RGA) spectra were only available up to a range of 100 atomic mass units (AMU). The base pressure during these experiments was approximately  $10^{-6}$  Torr. Since then we have improved our vacuum system by utilizing magnetically levitated turbo-molecular pumps. In addition, we have eliminated all organic components from the seals and the DPF system. Figure 16 shows an RGA spectrum obtained with an instrument with 200 AMU capability operated in the upgraded system. We can see that the primary peak is water vapor with little or no detectable hydrocarbons. The base pressure during these experiments was  $8 \times 10^{-8}$  Torr. The same multi-channel debris shield used in [5] was again employed in conjunction with a Si wafer witness sample. An experiment was conducted by exposing the debris shield and witness sample to the DPF plasma for 3 million pulses. All channels in the debris shield were oriented such that the EUV source was at the focal point of the debris shield. Wafers were analyzed using Auger- and ESCA- analysis. A coating of less than 5 nm thickness was observed for channels with 1 cm length and 2 mm diameter. The analysis showed that the coating contained carbon, oxygen, aluminum, and xenon.

No evidence of electrode material was seen, and the observed rate of carbon buildup was 100 times lower compared to the previous experiment [5].

These results underscore the need to correlate the observed rate of carbon deposition with reproducible features in the RGA spectrum. It is clear that we have made a considerable improvement to the system cleanliness as evidenced by the distinct reduction in base pressure and the reduced deposition rate. We have not yet identified all of the source terms for carbon in our system. This continues to be an area of active investigation. Future experiments will be conducted with additional levels of cleanliness handling using ultra-clean electro-polished vacuum vessels.

## 10. SUMMARY AND CONCLUSIONS

We have demonstrated a continuous improvement in the EUV in-band output of the DPF source. A summary of the parameters achieved with the DPF are shown in Figure 17. The highest in-band output power achieved to date with Xe gas is 76 W, obtained at a continuous repetition rate of 2000 Hz. In burst mode we have operated at 5 kHz with approximately 200 W of in-band power. The operation of the source in either positive or negative polarity has given us the ability to operate in a self-breakdown mode, or a pre-ionized mode with slightly different source parameters in each case. The trend in conversion efficiency for both positive and negative polarity operation seems to indicate a saturation at 0.5% with Xe gas. We have demonstrated successful operation of the DPF with Sn as the source element. At equivalent operating conditions approximately a four-fold increase in EUV output energy and CE was observed, compared to operation with Xe. The actual pulse energy measured with Sn was approximately 200 mJ per pulse at low repetition rate. We have improved our source metrology by implementing a source imaging system with a 45° incident angle ML mirror. The integrated CCD intensity results obtained with this diagnostics show excellent correlation on a pulse-to-pulse basis with the energy measured with a photodiode. This gives us a high degree of confidence that we are measuring the correct source size.

We are continuing to make progress on the thermal engineering of the pulsed-power system and discharge electrodes. With the changes outlined in the paper we expect to be able to operate the pulsed power system in a continuous mode at > 5 kHz repetition rate. The high degree of coupling of stored energy to the discharge (> 90%) enables us to operate with a lower total stored energy in the pulsed power system. The designs for electrode cooling tested so far have demonstrated the capability to extract > 21 kW of total discharge power from the electrode with > 11 kW from the smaller inner electrode. Results of the thermal modeling indicate that the present generation water-cooled electrodes should be thermally manageable up to 3 kHz in continuous operation.

The use of plasma modeling codes such as MHRDR has allowed us to explore some design space which is not easily accessible by experiment. A reasonable qualitative agreement has been observed between the variation of modeled and experimentally measured source parameters as a function of electrode length and gas pressure variations. Results of debris mitigation and potential optics contamination studies indicate that low levels of hydrocarbon contamination in the vacuum system continue to be a problem. Significant improvements in the control of the vacuum environment will be required to eliminate EUV- and DUV-catalyzed carbon growth on mirror surfaces.

## 11. ACKNOWLEDGEMENTS

We would like to thank all of the technicians on the EUVL technology development team without whose help this work would not have been possible. In particular we would like to acknowledge Miguel Jaramillo, Terrance Houston, Vi Phung, and Richard Taddiken for their help on this project. We also extend our thanks to members of our product development group for their input and to our excellent mechanical designer Ken LaValley who translated many of our ideas into workable designs.

## 12. REFERENCES

1. V. Banine and R. Moors, "Extreme ultraviolet sources for lithography applications", *Proc. of SPIE vol. 4343, Emerging Lithographic Technologies V*, ed. by E. A. Dobisz, p. 203 (2001).
2. W. Partlo, I. Fomenkov, R. Oliver, D. Bix, "Development of an EUV (13.5 nm) Light Source Employing a Dense Plasma Focus in Lithium Vapor", in *Proc. of SPIE vol. 3997, Emerging Lithographic Technologies IV*, ed. by E. A. Dobisz, p. 136 (2000).
3. W. N. Partlo, I. V. Fomenkov, R. M. Ness, R. I. Oliver, S. T. Melnychuk, and J. E. Rauch, "Progress Toward Use of a Dense Plasma Focus as a Light Source for Production EUV Lithography", in *Proc. of SPIE vol. 4343, Emerging Lithographic Technologies V*, ed. by E. A. Dobisz, p. 232 (2001).
4. I. Fomenkov, W. Partlo, R.M. Ness, I. Oliver, S. T. Melnychuk, O. Khodykin, N. Böwering, "Optimization of a Dense Plasma Focus Device as a Light Source for EUV Lithography", in *Proc. of SPIE vol. 4688, Emerging Lithographic Technologies VI*, ed. by R.L. Engelstad, p. 634 (2002).
5. I. V. Fomenkov, R. M. Ness, I. R. Oliver, S. T. Melnychuk, O. V. Khodykin, N. R. Böwering, C. L. Rettig, J. R. Hoffman, "Performance and Scaling of a Dense Plasma Focus Light Source for EUV Lithography", in *Proc. of SPIE vol. 5037, Emerging Lithographic Technologies VII*, ed. by R. L. Engelstad, p. 807 (2003).
6. Y. Kato, I. Ochiai, Y. Watanabe, and S. Murayama, *J. Vac. Soc. Technol.* **B6**, 195 (1988).
7. R. M. Ness and W. N. Partlo, "Solid-state pulsed power module (SSPPM) design for a dense plasma focus (DPF) device for semiconductor lithography applications", in *Proc. of the 13th IEEE Pulsed Power Plasma Science Conference, Las Vegas, NV, 2001*, p. 1268 (2002).
8. N. Böwering, M. Martins, W. N. Partlo, and I. V. Fomenkov, *J. Appl. Phys.* **95**, 16 (2004).
9. B. S. Bauer, R. C. Mancini, V. Makhin et al., "Development of magneto-hydrodynamic computer modeling of gas-discharge EUV sources for microlithography", these proceedings.

This work was partially funded by DARPA contract N66001-03-C-8017.

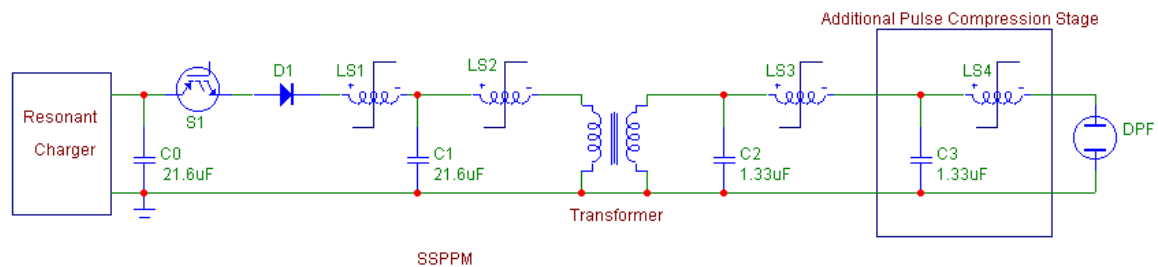


Figure 1. Schematic of the DPF pulsed power circuit. The present generation system is configured without the additional compression stage.

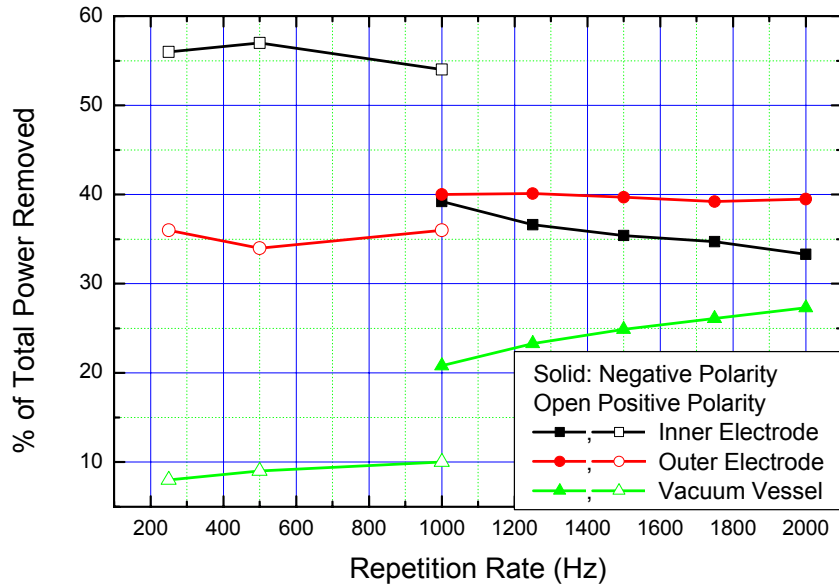


Figure 2. Power dissipation vs. repetition rate for PDPF and NDPF configurations.

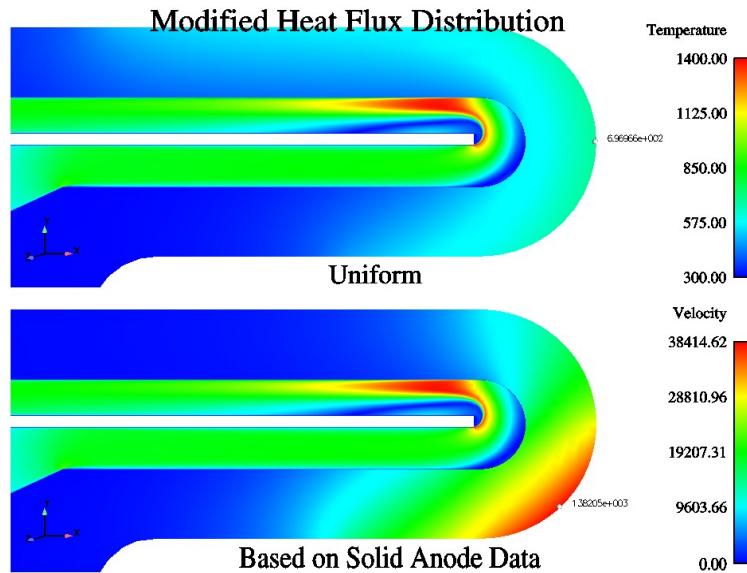


Figure 3. Thermal-hydraulic model results for single-channel water-cooled electrodes. The upper figure shows the temperature rise assuming a uniform heat distribution. The lower figure shows the temperature distribution using a heat flux obtained from thermographic measurements. Electrode wall temperatures are read from the upper legend, and channel flow velocities from the lower legend.

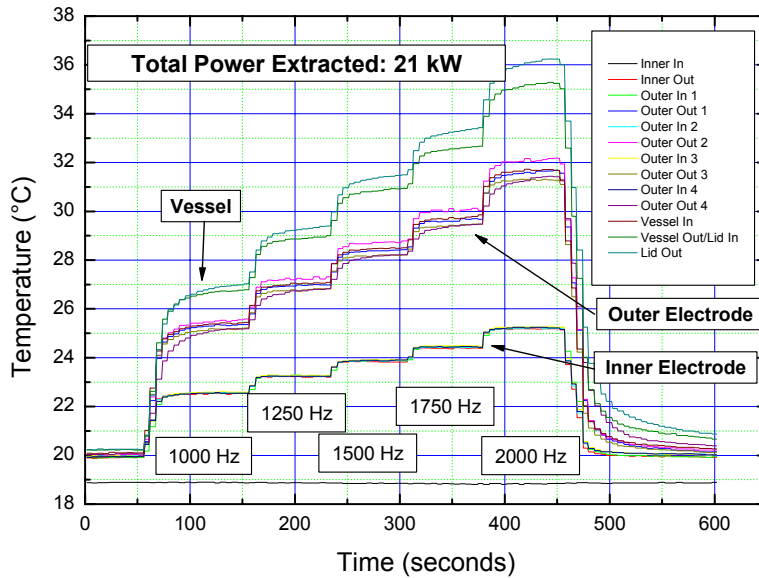


Figure 4. Rise of NDPF electrode temperature vs. time at increasing repetition rates. Lower curves: central electrode; middle curves: outer electrode; upper curves: vacuum vessel and lid.

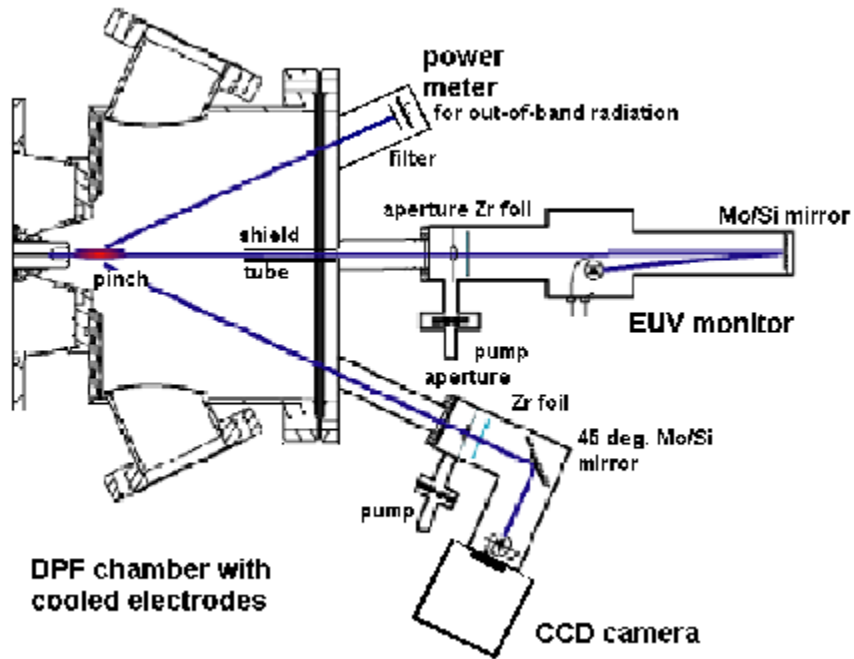


Figure 5. Schematics of the EUV metrology. Source imaging is performed with a CCD camera, a 45° ML mirror, a filter foil, and a pinhole aperture. EUV absolute energy is measured using a “standard” diode and ML mirror-based energy diagnostics.

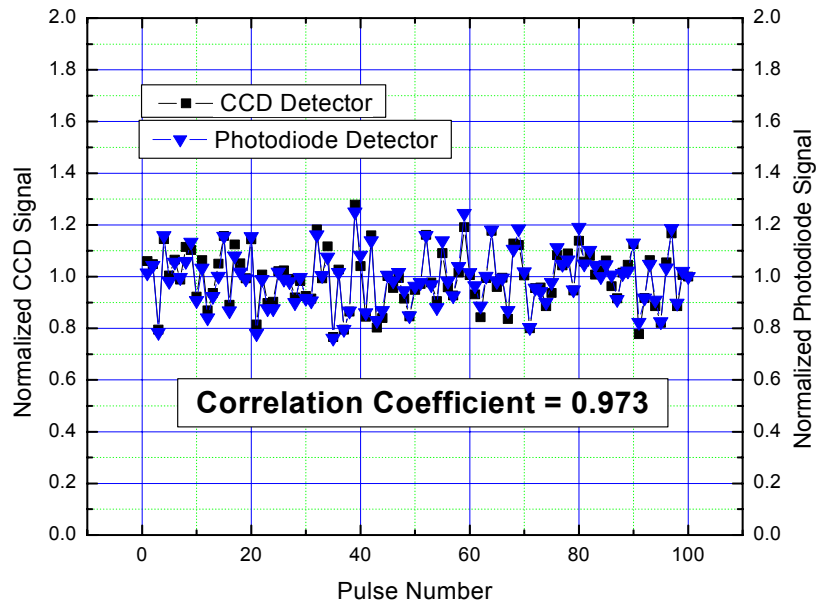


Figure 6. Correlation between the integrated CCD signal and the photodiode-based energy monitor.

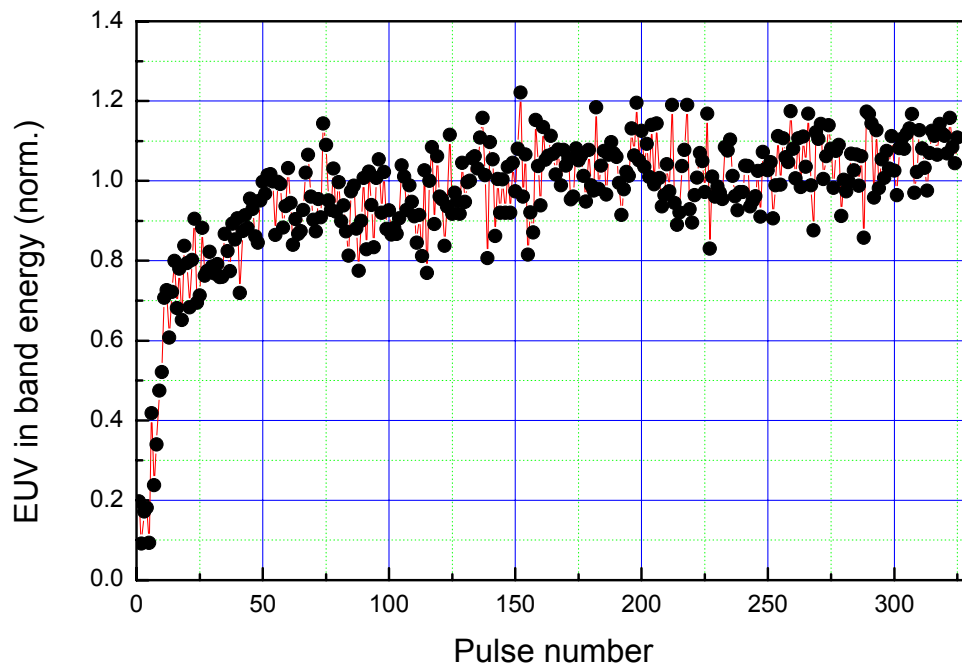


Figure 7. PDPF operation at 5 kHz for 325 pulses. The RMS energy stability disregarding the first 50 pulses is 8.6%.

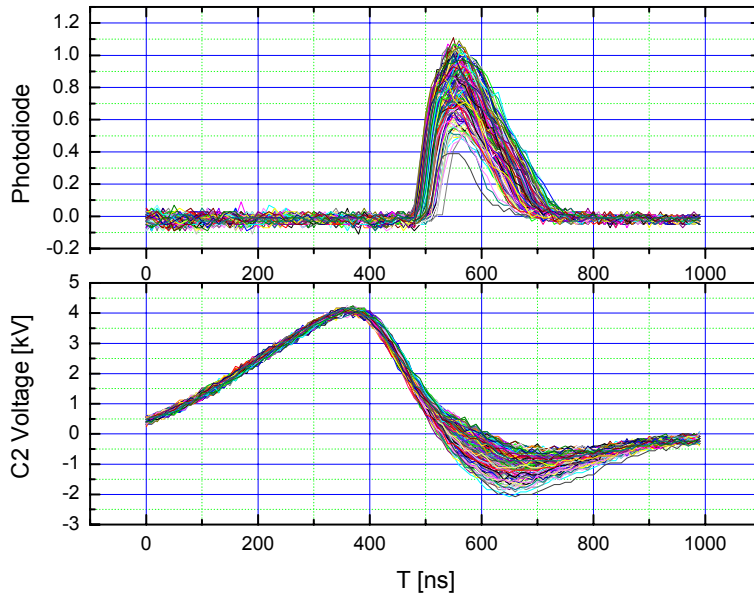


Figure 8. Photodiode and  $C_2$  voltage waveforms for burst operation at 4 kHz. The variation in the minimum  $C_2$  voltage shows the variation in coupling during a burst transient.

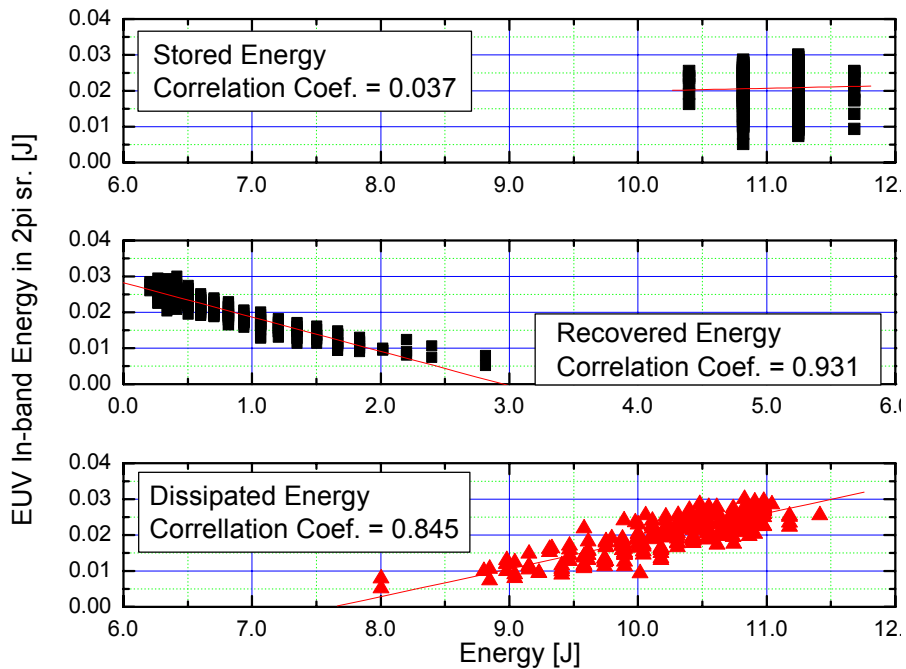


Figure 9. Correlation between the EUV in-band energy and the stored, recovered and dissipated energies, respectively, for the PDPF and operation at 4 kHz.

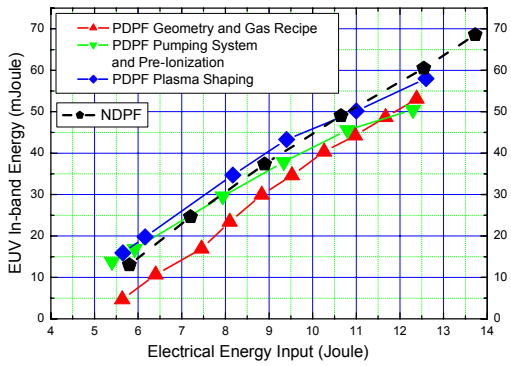


Figure 10. EUV in-band energy vs. input energy for positive and negative DPF operation.

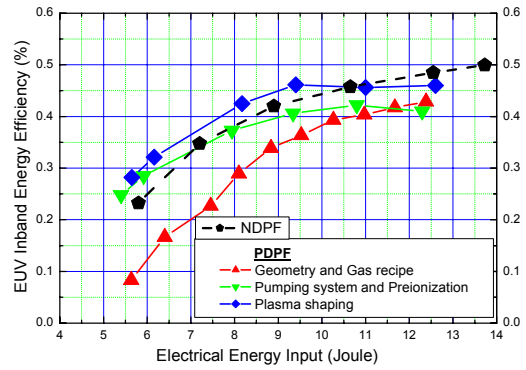


Figure 11. EUV in-band efficiency vs. input energy for positive and negative DPF operation.

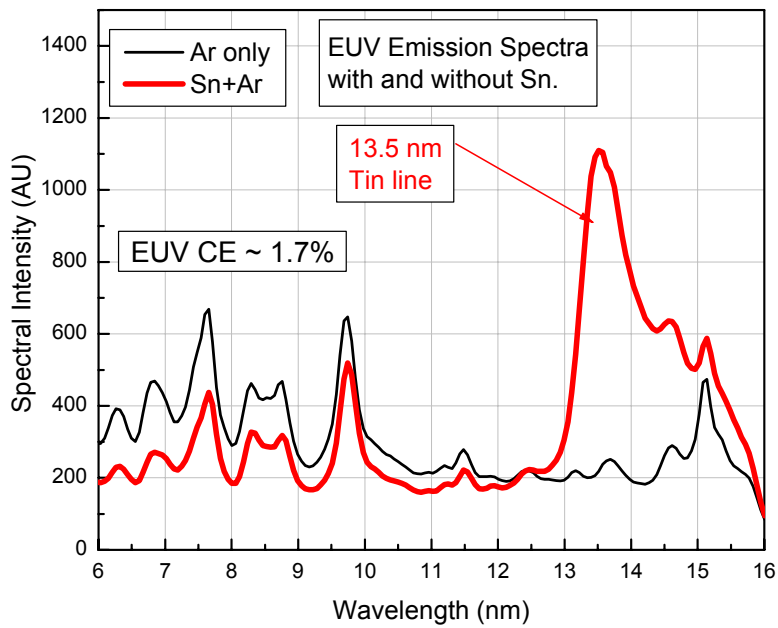


Figure 12. Emission spectrum of a NDPF discharge operated with pure Ar and Ar with Sn added. The data were obtained using a transmission grating spectrometer.

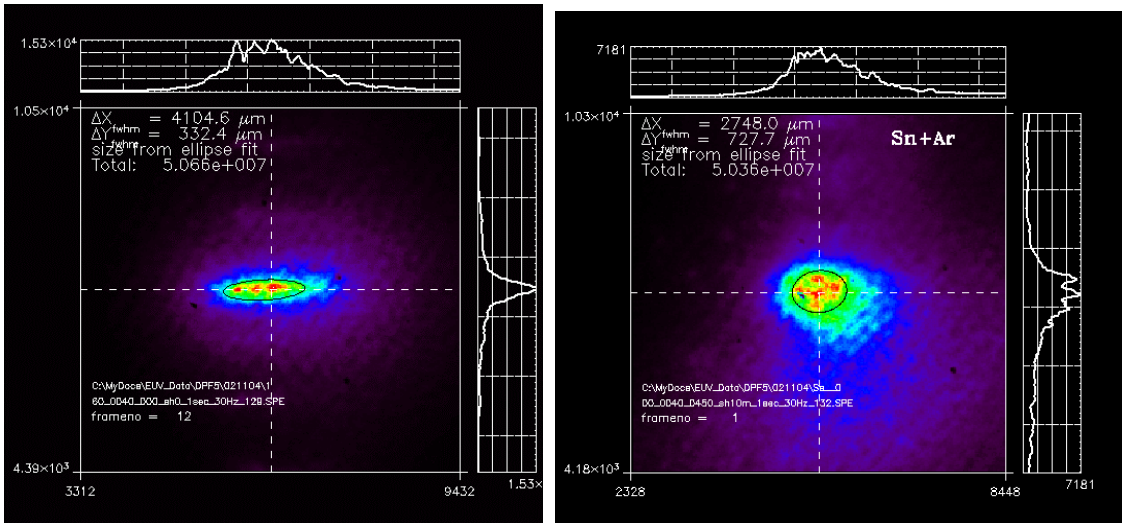


Figure 13. EUV in-band source image obtained with NDPF system. Left image: pure Xe; FWHM size: 4.1 mm x 0.33 mm; Right image: Sn with Ar; FWHM size: 2.75 mm x 0.72 mm.

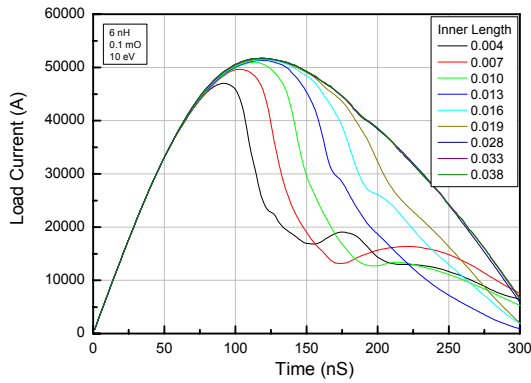


Figure 14. MHRDR simulation of load current waveform for various electrode lengths.

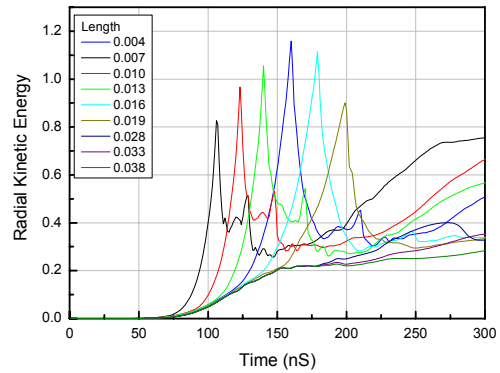


Figure 15. MHRDR simulation of radial kinetic energy vs. time for various electrode lengths.

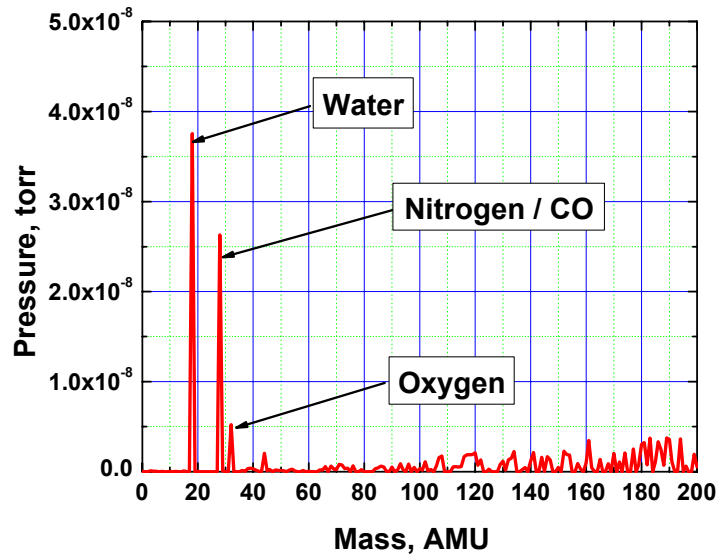


Figure 16. RGA spectrum of all-metal sealed DPF chamber with attached source, obtained with magnetically levitated turbo-molecular pump. Partial pressures: H<sub>2</sub>, 1e-9 Torr; H<sub>2</sub>O, 4e-8 Torr; N<sub>2</sub>, CO, 3e-8 Torr; O<sub>2</sub>, 5e-9 Torr; CO<sub>2</sub>, 2e-9 Torr.

	Xenon	Sn
<b>EUV efficiency (2% BW, 2π sr)</b>	~0.50%	~1.7%
<b>EUV energy per pulse (2% BW, 2π sr)</b>	~ 70 mJ	~200mJ
<b>Average source size (FWHM)</b>	~ 0.33 x 4.1 mm	~0.73 x 2.75 mm
<b>Source position stability (centroid)</b>	< 0.05 mm, rms	
<b>Continuous repetition rate</b>	2300 Hz	30 Hz
<b>Burst repetition rate</b>	5000 Hz	500 Hz
<b>Energy Stability</b>	~ 7 %, rms	
<b>Avg. EUV Output Power (2% BW, 2π sr)</b>	76 Watt	6 Watt
<b>EUV Output Power, Burst (2% BW, 2π sr)</b>	200 Watt	> 50 Watt

Figure 17. Summary of the characteristic data obtained for Xe and Sn.